THE JOURNAL OF PHYSICAL CHEMISTRY LETTERS
A JOURNAL OF THE AMERICAN CHEMICAL SOCIETY

pubs.acs.org/JPCL

Letter

Subsecond Three-Dimensional Nitrogen-15 Magnetic Resonance Imaging Facilitated by Parahydrogen-Based Hyperpolarization

Alexandra I. Trepakova,* Ivan V. Skovpin, Nikita V. Chukanov, Oleg G. Salnikov, Eduard Y. Chekmenev, Andrey N. Pravdivtsev, Jan-Bernd Hövener, and Igor V. Koptyug*

Cite This: *J. Phys. Chem. Lett.* 2022, 13, 10253−10260

Read Online

ACCESS | Metrics & More | Article Recommendations | Supporting Information

ABSTRACT: Magnetic resonance imaging (MRI) provides unique information about the internal structure and function of living organisms in a non-invasive way. The use of conventional proton MRI for the observation of real-time metabolism is hampered by the dominant signals of water and fat, which are abundant in living organisms. Heteronuclear MRI in conjunction with the hyperpolarization methods does not encounter this issue. In this work, we polarized ^{15}N nuclei of [$^{15}N_1$]fampridine (a drug used for the treatment of multiple sclerosis) to the level of 4% in nuclear magnetic resonance (NMR) experiments and 0.7% in MRI studies using spin-lock-induced crossing combined with signal amplification by reversible exchange. Consequently, three-dimensional ^{15}N MRI of the hyperpolarized ^{15}N-labeled drug was acquired in 0.1 s with a signal-to-noise ratio of 70. In addition, the NMR signal enhancements for ^{15}N-enriched fampridine and fampridine with a natural abundance of ^{15}N nuclei were compared and an explanation for their difference was proposed.

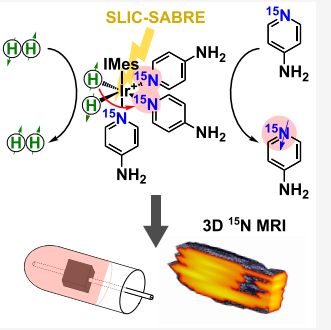

Magnetic resonance imaging (MRI) is widely employed for structural, functional, and dynamics studies, including studies of chemical reactions *in situ*.[1−5] The interest in using MRI methods is driven by medical diagnostics centers, which utilize a non-invasive MRI technology due to its rich information content.[6] Now, with the help of MRI, it is possible to study the pathologies of organs, the structure of tissues, and various biological processes occurring inside living organisms.[7−11] The most frequently used nuclei in MRI studies are ^{1}H, ^{31}P, and ^{19}F with high natural abundance (99.9885% for ^{1}H and 100% for ^{31}P and ^{19}F)[12] and high gyromagnetic ratios [$\gamma(^{1}H) \approx 42.6$ MHz/T, $\gamma(^{31}P) \approx 17.2$ MHz/T, and $\gamma(^{19}F) \approx 40.1$ MHz/T]. As a result of the favorable nuclear spin properties, the signals of these nuclei can be readily observed in a typical *in vivo* MRI examination.[6,13−18] However, MRI methods do not reveal their full potential due to their relatively low sensitivity in comparison to computed tomography (CT) and optical imaging methods. Over the years, MRI technology has been considerably improved to remedy the sensitivity limitations. Despite the substantial technological advances such as the widespread use of 3 T MRI scanners and the clinical advent of 7 T MRI scanners, clinical applications have been largely limited to ^{1}H detection. However, heteronuclear MRI can fundamentally yield complementary or even unique information about metabolism and drug distribution in living organisms, primarily because of the zero- or low-background signals of heteronuclei such as ^{19}F, ^{13}C, ^{15}N, etc. An additional favorable property of heteronuclei (e.g., ^{19}F, ^{13}C, and ^{15}N) is their large chemical shift dispersion,[19] which can further expand the range of possible MRI applications such as the differentiation of metabolites. The main reason for the lack of ^{15}N biomedical studies, in particular, is the low detection sensitivity caused by the ^{15}N isotope natural abundance of only 0.364% and its low $\gamma(^{15}N)$ of −4.32 MHz/T (note that conventional MR sensitivity scales approximately as γ^3).[20]

Both of the sensitivity-limiting factors discussed above (a low natural abundance of some nuclear isotopes and low sensitivity) can be remedied. First, ^{15}N isotopic labeling of an endogenous contrast agent can be readily applied[21] to [$^{15}N_2$]imidazole,[22,23] [$^{15}N_1$]nicotinamide,[24,25] [$^{15}N_2$]- and [$^{15}N_3$]metronidazole,[26] and many others. The partial solution for the second challenge is the use of hyperpolarization methods. In recent years, several hyperpolarization techniques opened new opportunities for the MRI community because they make it possible to enhance nuclear spin polarization [and correspondingly nuclear magnetic resonance (NMR) signal] by ≤5 orders of magnitude.

All hyperpolarization methods are based on creating a non-equilibrium state with the difference between nuclear spin sublevel populations much greater than that at thermal equilibrium. Signal amplification by reversible exchange (SABRE)[27] is one of these revolutionary hyperpolarization methods. It is based on the use of parahydrogen (p-H_2) as a

Received: September 1, 2022
Accepted: October 24, 2022
Published: October 27, 2022

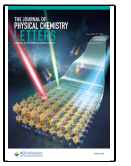

source of nuclear spin order. In SABRE, hyperpolarization is continuously created as a result of a reversible exchange of a to-be-hyperpolarized substrate molecule and p-H_2 between the catalytic complex and the bulk "free" solute.[27] The SABRE technique was pioneered in 2009,[27] and it gained popularity over the years because of its simplicity, efficiency, and low cost compared with other hyperpolarization techniques such as spin exchange optical pumping (SEOP)[28,29] or dissolution dynamic nuclear polarization (d-DNP).[30,31] To date, SABRE demonstrated its power to hyperpolarize, among many other targets, the FDA-approved drug metronidazole with a ^{15}N polarization level of >50%.[32] An additional beneficial feature of SABRE is that the molecular structure of the to-be-hyperpolarized exchangeable substrate molecule does not change as a result of the process of hyperpolarization. However, it should be noted that for *in vivo* applications of SABRE, the catalytic polarization transfer complex has to be removed from the hyperpolarized solution before its administration.[33−37]

While SABRE was originally developed as an efficient ^{1}H hyperpolarization method,[38,39] approaches to transfer spin order from p-H_2-derived hydrides to heteronuclei such as ^{13}C or ^{15}N were promptly developed.[40−42] An additional benefit of heteronuclei in hyperpolarization studies is alonger T_1 relaxation time compared to those of ^{1}H nuclei. There are two main strategies for the spin order transfer from p-H_2-derived hydrides to the heteronucleus of choice: "spontaneous" polarization transfer by free evolution at a given field and spin order transfer by radiofrequency (RF) pulse sequences. In the first case, the spins are exposed to ultralow magnetic fields, where spin order is spontaneously distributed among all coupled spins (μ-metal magnetic shields are employed to create desired fields on the order of nano- or microteslas).[43−46] Then the sample is transferred from the magnetic shield to an NMR or MRI instrument for signal detection. In the second approach, sequences of RF pulses induce the desired spin order transfer, while the sample is residing within the probe of an NMR or MRI instrument. There are many demonstrated pulse sequences for achieving this polarization transfer, for example, LIGHT-SABRE,[41] SABRE-INEPT,[23] QUASR-SABRE,[47,48] and SLIC-SABRE.[49,50] These pulse sequences allow enhancement of ^{15}N polarization by several orders of magnitude.

In this study, we used ^{15}N-labeled 4-amino[^{15}N]pyridine[51] [fampridine, [^{15}N$_1$]FAM (Figure 1A)] as a model for hyperpolarized ^{15}N molecular imaging. FAM has therapeutic value for controlling symptoms of demyelinating diseases and disorders of neuromuscular transmission.[52] It restores conduction in demyelinated axons through blockage of potassium (K^+) channels and enhances neuroneuronal or neuromuscular transmission in normally myelinated neurons through an increase in calcium (Ca^{2+}) influx.[52,53] [^{15}N$_1$]FAM is thus attractive as a potential novel probe for molecular MRI.

In our previous studies, we demonstrated the possibility of using SLIC-SABRE to hyperpolarize the ^{15}N nucleus of FAM[54] at the natural abundance of the ^{15}N isotope. The SLIC-SABRE (Figure 1B) pulse sequence is based on the effect of spin-lock induced crossing (SLIC), pioneered by DeVience et al.[55] The SLIC-SABRE pulse sequence is similar to that of LIGHT-SABRE (low-intensity generation of high-tesla SABRE),[41] where a low-power continuous wave pulse causes polarization transfer. However, SLIC-SABRE represents an improved variant, where the influence of singlet−triplet spin state mixing on the catalyst complex is taken into account.[50] This feature makes SLIC-SABRE more robust and efficient than LIGHT-SABRE. In the previous work, we were able to demonstrate ^{15}N polarization $p(^{15}\mathrm{N}) \sim 8\%$ using SLIC-SABRE, which allowed us to perform two-dimensional (2D) ^{15}N MRI with a spatial resolution of 0.3 × 2.4 mm^2/pixel in <1 s. However, despite the significant improvement of signal intensity, three-dimensional (3D) ^{15}N MRI was not achieved. In this work, we extended the frontiers of ^{15}N MRI further by demonstrating the feasibility of subsecond 3D ^{15}N MRI using hyperpolarized [^{15}N$_1$]FAM. Using 99% ^{15}N-labeled [^{15}N$_1$]FAM and SLIC-SABRE, we achieved 0.7% ^{15}N polarization with a 9.4 T microimaging NMR spectrometer and 4% ^{15}N polarization with a 7 T NMR spectrometer.

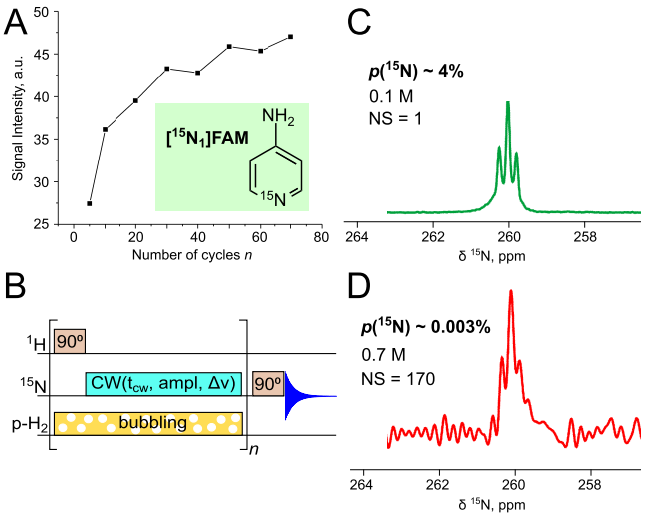

Figure 1. (A) ^{15}N NMR signal as a function of the number of spin order transfer cycles n in the SLIC-SABRE sequence. The inset shows the chemical structure of [^{15}N$_1$]FAM. (B) Schematics of the SLIC-SABRE pulse sequence. (C) Single-scan ^{15}N NMR spectrum of hyperpolarized 0.1 M [^{15}N$_1$]FAM in methanol-d_4 at a 9.4 T magnetic field. (D) ^{15}N NMR spectrum of thermally polarized 0.7 M [^{15}N$_1$]FAM in methanol-d_4 at 9.4 T MRI using 170 signal accumulations acquired with a 5 min repetition time.

In all experiments, an iridium N-heterocyclic carbene complex [Ir(COD)(IMes)Cl] [IMes = 1,3-bis(2,4,6-trimethylphenyl)imidazole-2-ylidene, and COD = 1,5-cyclooctadiene] was used as a SABRE precatalyst. This complex was prepared from commercially available precursors, [Ir(COD)Cl]$_2$ and [IMes]$^+$[BF$_4$]$^-$, according to the previously described method.[56] [^{15}N$_1$]FAM was synthesized according to the procedure reported elsewhere.[51] NMR spectra were recorded using a 300 MHz (B_0 = 7 T) spectrometer equipped with a 10 mm probe or using a 400 MHz (B_0 = 9.4 T) microimaging instrument equipped with a 25 mm two-channel probe (^{1}H and ^{15}N) and a gradient strength of ≤150 G/cm. A 0.1 M solution of [^{15}N$_1$]FAM with 5 mM [Ir(COD)(IMes)Cl] precatalyst was used for SLIC-SABRE.

Two important elements in the SLIC-SABRE pulse sequence are (i) spin order transfer and (ii) signal acquisition. Spin order transfer utilizes a 90° ^{1}H RF pulse followed by a continuous wave (CW) pulse tuned to the ^{15}N resonance of the bound equatorial [^{15}N$_1$]FAM (Figures 1B and 2). The CW pulse has the following parameters: duration (t_{cw}), amplitude (A), and an offset from the frequency of the bound substrate ($\Delta\nu = \nu_{rf} - \nu_{bound}$). The polarization transfer block was repeated n times to attain a higher ^{15}N polarization of free [^{15}N$_1$]FAM. The signal of hyperpolarized [^{15}N$_1$]FAM was

https://doi.org/10.1021/acs.jpclett.2c02705
J. Phys. Chem. Lett. 2022, 13, 10253−10260

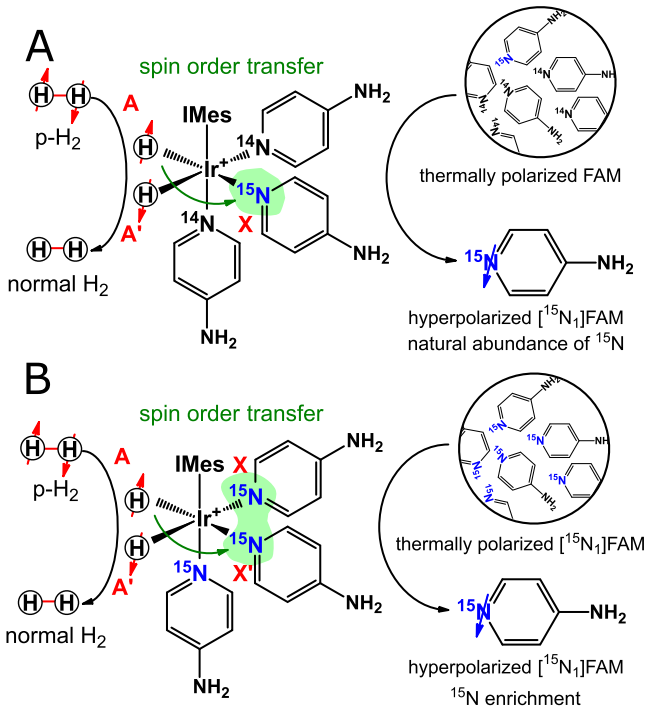

Figure 2. Simple mechanistic model of SABRE chemical exchange and spin order transfer to (A) FAM with a natural abundance (0.364%) of ^{15}N nuclei and (B) ^{15}N-enriched FAM. In the first case, 98.9% of Ir complexes have three [^{14}N$_1$]FAM ligands and only 0.73% of Ir complexes have at least one equatorial [^{15}N$_1$]FAM ligand. Only the latter complexes are responsible for the spin order transfer from p-H$_2$ to ^{15}N. When a substrate is 99% enriched in ^{15}N, the spin order is distributed in almost every Ir complex including two ^{15}N nuclei.

obtained by applying a 90° RF pulse on the ^{15}N channel followed by a free induction decay acquisition for an NMR spectroscopy experiment or by using an imaging pulse sequence for an MRI experiment. During SLIC-SABRE, p-H$_2$ was continuously supplied during spin order transfer and the bubbling was terminated shortly before signal acquisition to prevent the sample inhomogeneity and concomitant spatial distortions of the magnetic field.

In the previous studies, we optimized ^{15}N SLIC-SABRE performance by changing the following parameters: A, $\Delta\nu$, t_{cw}, n, the rate of p-H$_2$ gas supply (Q), and the sample temperature (T).[49,54] It was shown that all studied heterocyclic compounds ([^{15}N]pyridine, [^{15}N$_1$]nicotinamide, and fampridine) had the same optimal CW pulse amplitude (A = 5 Hz) and duration (t_{cw} = 1.17 s).[49] However, the frequency offset depends on the experimental conditions and has to be optimized each time before the experiments; the common offset was approximately 17−18 Hz. The other optimized parameters were the same as in the previous study.[54] For a proper comparison, we list here all essential parameters of the SLIC-SABRE experiment: t_{cw} = 1.17 s, A = 5 Hz, n = 40, Q = 80 sccm, and T = 293 K. The sample was loaded into a standard 5 mm NMR tube and placed into a 7 T NMR spectrometer before the experiment. The 82% enriched p-H$_2$ gas was bubbled through the sample at a pressure of 4.4 bar.

Using these parameters, we achieved a ^{15}N signal enhancement $\varepsilon(^{15}\mathrm{N})$ of ∼16000 corresponding to a ^{15}N polarization $p(^{15}\mathrm{N})$ of ∼4%. Interestingly, this value is 2 times lower than that previously obtained for nonlabeled FAM [$p(^{15}\mathrm{N})$ = 8%, and $\varepsilon(^{15}\mathrm{N})$ ∼ 32000] under similar experimental conditions.[54]

Such a difference can be rationalized using a simple mechanistic model of SABRE (Figure 2). When FAM with a natural abundance of ^{15}N nuclei is employed in SABRE experiments, the probability that two or three substrate molecules in the SABRE complex have a ^{15}N label is rather small. Therefore, the spin system relevant for spin order transfer can be approximated by three spins [AA′X (Figure 2A)]: two ^{1}H nuclei of p-H$_2$-derived hydrides and one ^{15}N nucleus.[44] At the same time, when ^{15}N-labeled [^{15}N$_1$]FAM is used, all three Ir metal-coordinated substrate molecules contain a ^{15}N nucleus; i.e., there are three ^{15}N nuclei in the SABRE complex. Note that the J coupling network and chemical exchange favor spin order transfer from p-H$_2$ to only two substrate molecules at equatorial positions, while the axial substrate is almost SABRE-inactive due to negligible spin−spin couplings of its nuclei to hydrides and extremely slow exchange with the pool of free substrate molecules. Hence, in this case, the spin order is transferred from p-H$_2$-derived hydrides to two ^{15}N nuclei in the four-spin AA′XX′ system (Figure 2B).[45]

For a quantitative analysis of SLIC-SABRE for the substrates with a natural abundance of ^{15}N and those enriched with ^{15}N isotopes, we used a "quantitative SABRE model",[57] which was successfully applied in our previous SLIC-SABRE studies.[49,58] According to this model, the SABRE process is reduced to a two-stage exchange:[49]

$$\mathrm{MH_2S_2} \xrightarrow{k_d} \mathrm{MH_2} + \mathrm{S_2} \tag{1}$$

$$\mathrm{MH_2^*} + \mathrm{S_2} \xrightarrow{k_a'} \mathrm{MH_2S_2} \tag{2}$$

where M is the core of the organometallic complex [e.g., Ir(IMes)S], MH_2 is a short-lived intermediate with two equatorial substrates missing, and MH_2 immediately converts to MH_2^* with H_2^* being pure p-H$_2$. This model was employed to describe spin dynamics in the case of isotopically labeled [^{15}N$_1$]FAM. For the case of unlabeled FAM, we used a different model

$$\mathrm{MH_2ZS} \xrightarrow{k_d/2} \mathrm{MH_2Z} + \mathrm{S} \tag{3}$$

$$\mathrm{MH_2^*Z} + \mathrm{S} \xrightarrow{k_a'^{na}} \mathrm{MH_2ZS} \tag{4}$$

where Z and S are [^{14}N$_1$]FAM and [^{15}N$_1$]FAM, respectively. We note that these models simplify the SABRE processes, but these simplifications are inevitable because the more realistic models are dramatically more time-consuming (see the details in the Supporting Information). The differences between the two models were introduced to account for the differences in spin dynamics in the cases of labeled and unlabeled substrates (see the Supporting Information).

Using this model, we simulated SLIC-SABRE and equilibrium $p(^{15}\mathrm{N})$ for the corresponding AA′X and AA′XX′ spin systems described above, and the details are presented in the Supporting Information. The ratio of $p(^{15}\mathrm{N})$ levels reaches 2 for the fast exchange rates k_d ∼ 50 s^{-1} (i.e., in good qualitative agreement with experimental observation), and this ratio is close to 1 for the slow exchange with k_d ∼ 1 s^{-1}. We employed the parameters listed in Table 1 to obtain the simulation results shown in Figure 3. We note that k_d values used in simulations cannot be directly compared with dissociation rate constants measured using EXSY. It is noteworthy that in the previous study[51] the dissociation rate constant for FAM was estimated to be 3.4 s^{-1} at room

https://doi.org/10.1021/acs.jpclett.2c02705
J. Phys. Chem. Lett. 2022, 13, 10253−10260

Table 1. SABRE System Parameters Used for SLIC-SABRE Simulations

system	chemical shift (ppm)	high-field T_1 relaxation time (s)[a]	J coupling constant (Hz)
$H_2{}^{15}N$	MH_2ZS (−22, −22, 200)	MH_2ZS (1, 1, 6)	MH_2ZS
	S (300)	S (60)	$J^2_{HH} = -7.7$ $J^{2,trans}_{HN} = -20.9$ $J^{2,cis}_{HN} = 0.6$
$H_2{}^{15}N_2$	MH_2S_2 (−22, −22, 200, 200)	MH_2S_2 (1, 1, 6, 6)	MH_2S_2
	S_2 (300, 300)	S_2 (60, 60)	$J^2_{HH} = -7.7$ $J^{2,trans}_{HN} = -20.9$ $J^{2,cis}_{HN} = 0.6$ $J^2_{NN} = 0.4$

[a]Because the precise experimental measurement of the T_1 values for the free and coordinated substrate is hardly possible because of the chemical exchange, the presented estimated values were utilized for simulations.

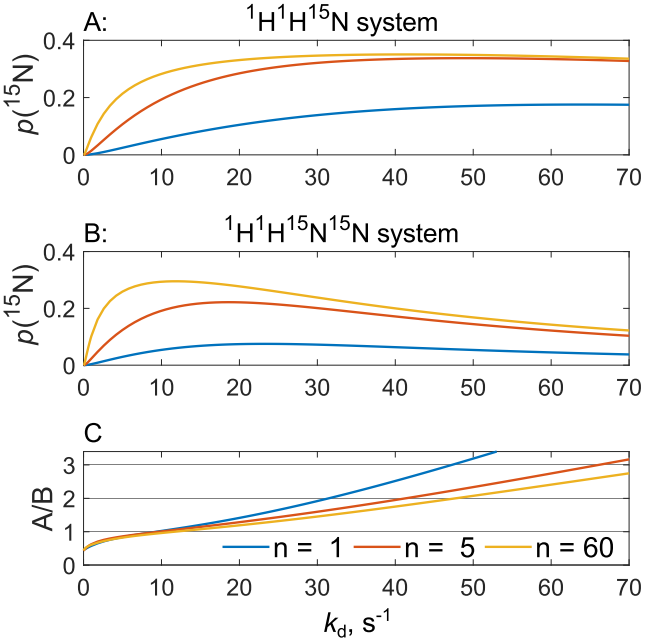

Figure 3. Simulated ^{15}N polarization in SLIC-SABRE spin order transfer for (A) $MH_2ZS = H_2{}^{15}N$ and (B) $MH_2S_2 = H_2(^{15}N)_2$ spin systems and (C) their ratio as a function of k_d. All relevant spin system parameters are listed in Table 1. SLIC-SABRE parameters ν_{rf} = 200 ppm + $\Delta\nu$, $\Delta\nu$ = 18 Hz, A = 5 Hz, t_{cw} = 1.17 s, and B_0 = 7 T and eq S6 (A) and eq S7 (B) were used for calculation. No additional delays and an ideal ^1H 90° RF pulse were considered. The system had a period of free evolution of 100 s before SLIC-SABRE. The concentration ratio was $\frac{[MH_2S_2]}{[S]} = \frac{1}{17}$ (see the Supporting Information for details). The numbers in the legend are the numbers of SLIC-SABRE cycles (n = 1, 5, and 60).

temperature, while the simulations reported here predict that when $k_d = 3.4\ s^{-1}$ the levels of ^{15}N polarization of labeled and unlabeled FAM should be almost similar. The simulations are detailed in the Supporting Information. The overall discrepancy between the simulations and the experiments is readily explained by less than perfect experimental conditions. In the simulations, it was assumed that the reservoir of p-H_2 is unlimited, while experimentally p-H_2 mixing and flow rate may be insufficient to reach the full potency of the polarization process.[44] Moreover, the simulations oversimplified the SABRE chemical exchange of the substrate and p-H_2 and did not account for possible differences in relaxation times of nuclear spins in the polarization transfer complex in the case of labeled and unlabeled FAM. The SABRE model with fewer simplifications that considers the chemical exchange of two substrates was proposed before.[59] However, this model is inevitably nonlinear and hence very time-consuming and requires more system parameters, which have not yet been identified; therefore, only the simplified model was utilized here.

Despite a lower signal enhancement and $p(^{15}N)$, the overall ^{15}N signal intensity was greater for enriched [$^{15}N_1$]FAM than for natural-abundance FAM because the molar polarization was >100 times higher for [$^{15}N_1$]FAM (0.04 × 85 mM × 0.99 ≈ 3.366 mM, where 0.99 is the ^{15}N enrichment level and 0.04 is the ^{15}N polarization achieved at 7 T NMR) than that for FAM (0.08 × 85 mM × 0.00364 ≈ 0.025 mM, where 0.00364 is a natural abundance of ^{15}N and 0.08 was the ^{15}N polarization achieved at 7 T NMR[54]).

While the evaluation of the ^{15}N NMR signal enhancement reported above was performed on a 7 T NMR spectrometer, subsequent MRI experiments were performed on a 9.4 T MR microimaging instrument. Thus, it was necessary to modify the experimental setup and optimize the experimental parameters again. As a consequence of the optimization and setup adjustment for imaging studies, $\epsilon(^{15}N)$ was decreased to ~2000 [$p(^{15}N)$ = 0.7%] for a 0.1 M solution of [$^{15}N_1$]FAM with 5 mM Ir precatalyst in methanol-d_4 (Figure 1C,D). The resulting 2D ^{15}N MR image with a signal-to-noise ratio (SNR) of 70 is presented in Figure 4B.

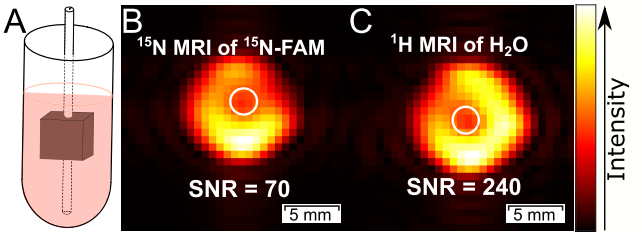

Figure 4. (A) Schematic drawing of the imaging phantom, (B) 2D ^{15}N FLASH MRI of hyperpolarized 0.1 M [$^{15}N_1$]FAM, and (C) 2D ^1H FLASH MRI of 0.1 M H_2O in D_2O. The imaging phantom consists of a 10 mm NMR tube with a methanol-d_4 solution of 0.1 M [$^{15}N_1$]FAM, a capillary for parahydrogen supply, and a plastic cube attached to the capillary. For both experiments, a 10 mm NMR tube with an inner diameter of 8.76 mm was filled with 2.5 mL of a SABRE mixture solution and placed in the isocenter of a 9.4 T vertical bore MRI magnet. The glass capillary inside the NMR tube is also visible in the MR images (indicated by white circles).

Such a substantial decrease in polarization was likely caused by switching from a 5 mm NMR tube to a 10 mm NMR tube, where solution mixing with p-H_2 is less efficient even after optimization of the p-H_2 flow rate (Figure S1B) because of a greater liquid volume and the presence of a plastic cubic phantom in the NMR tube (Figure 4A). An additional factor is the greater inhomogeneity of B_0 and B_1 magnetic fields; the effect of the latter on the spin order transfer was discussed recently in ref 60, and a much smaller sample size was recommended to have a homogeneous B_1 for a similar system. The SLIC spin order transfer technique utilizes small

https://doi.org/10.1021/acs.jpclett.2c02705
J. Phys. Chem. Lett. 2022, 13, 10253−10260

amplitude (A = 5 Hz) RF pulses; hence, the B_0 magnetic field inhomogeneity of the same magnitude or larger will result in a substantial reduction of polarization. The full width at half-maximum for ^{15}N during p-H_2 bubbling was 16 Hz.

Comparison of a ^{15}N MRI scan of 0.1 M hyperpolarized [$^{15}N_1$]FAM in methanol-d_4 with a ^{1}H MRI scan of a reference 0.1 M H_2O in D_2O showed that the SNR was only ~3.4 times higher for ^{1}H MRI of H_2O than for ^{15}N MRI of [$^{15}N_1$]FAM using similar pulse sequence parameters optimized for each channel individually. This fact is particularly remarkable because the sensitivity difference between ^{1}H and ^{15}N is ~1000-fold taking into account only the difference in their γ value.

Considering that the relaxation time of ^{15}N nuclei in [$^{15}N_1$]FAM at 9.4 T was rather long [27 ± 3 s (see the Supporting Information)], the SNR of 70 was achieved for only 0.7% ^{15}N polarization, and no background signal is present, ^{15}N MRI of hyperpolarized [$^{15}N_1$]FAM has a potential to provide more information than conventional ^{1}H MRI and to shed light on metabolic processes *in vivo*.

We have also obtained a 3D ^{15}N MR image (Figure 5) with a spatial resolution of 0.5 × 5 × 5 mm^3/pixel and a maximum

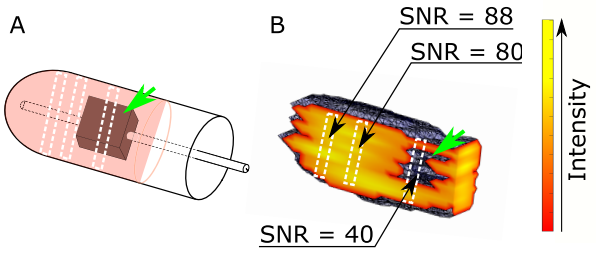

Figure 5. (A) Schematic drawing of the imaging phantom and (B) 3D ^{15}N MR image of hyperpolarized [$^{15}N_1$]FAM. The imaging phantom consists of a 10 mm NMR tube with a methanol-d_4 solution of 0.1 M [$^{15}N_1$]FAM, the capillary for parahydrogen supply, and the plastic cube. The 3D ^{15}N MR image was acquired in 0.1 s after SLIC-SABRE at 9.4 T. For a better presentation, the resulting 3D rendering is cut by two planes (Z–Y, along the tube, and X–Y, across the tube). The area with zero signal corresponds to the position of the plastic cube; it is also marked with a green arrow. The dashed rectangles schematically correspond to different X–Y slices (20, 25, and 35) on both panels A and B, and the highest SNR values in each slice are given in panel B.

SNR of ~150; the SNR values for some X–Y slices are given in Figure S3. The resulting images were zero-filled to a matrix size of 128 × 64 × 64 for better presentation. Both the tube and the phantom were well resolved.

In conclusion, we have reported on ^{15}N SLIC-SABRE hyperpolarization of ^{15}N-labeled [$^{15}N_1$]fampridine. Although the experimentally observed polarization levels for isotopically labeled fampridine were ~2-fold lower than at the natural abundance of ^{15}N nuclei (as supported by simulations), the ^{15}N enrichment provided an overall ~140-fold increase in molar polarization. This strong ^{15}N NMR signal was successfully employed for the demonstration of the feasibility of subsecond 3D ^{15}N MRI. Our further plans include the addition of spectroscopic data in each voxel, which definitely will increase imaging time but will undoubtedly provide the chemical shift dimension needed for future metabolic sensing studies. Future studies will also need to address the problem of the removal of the toxic catalyst from the solution while preserving ^{15}N hyperpolarization. This work expands the opportunities for molecular imaging in biological systems, and for instance, ^{15}N MRI of [$^{15}N_1$]FAM can be potentially employed for the detection of demyelinated regions of the brain. Although the standard clinical MRI scanners currently do not possess heteronuclear RF pulsing and detection capabilities, the heteronuclear MRI technology is available with instruments used for preclinical research and is being successfully developed and utilized at a number of research sites worldwide.[61−64] Future developments of heteronuclear MRI applications will facilitate the commercial availability of the required equipment.

■ ASSOCIATED CONTENT

Supporting Information

The Supporting Information is available free of charge at https://pubs.acs.org/doi/10.1021/acs.jpclett.2c02705.

All experimental details, optimization of the SLIC-SABRE pulse sequence, calculation of signal enhancement, and measurements of T_1 relaxation times and SNR values for different slices of a 3D model (PDF)

MOIN spin library (https://www.moincc.de/method-development/mr/moin-spin-library) with the used spin order transfer simulation scripts (ZIP)

■ AUTHOR INFORMATION

Corresponding Authors

Alexandra I. Trepakova − *International Tomography Center, SB RAS, Novosibirsk 630090, Russia; Novosibirsk State University, Novosibirsk 630090, Russia; Institute of Cytology and Genetics, SB RAS, Novosibirsk 630090, Russia;* orcid.org/0000-0003-3440-6677; Email: alexandra.svyatova@tomo.nsc.ru

Igor V. Koptyug − *International Tomography Center, SB RAS, Novosibirsk 630090, Russia;* orcid.org/0000-0003-3480-7649; Email: koptyug@tomo.nsc.ru

Authors

Ivan V. Skovpin − *International Tomography Center, SB RAS, Novosibirsk 630090, Russia*

Nikita V. Chukanov − *International Tomography Center, SB RAS, Novosibirsk 630090, Russia; Novosibirsk State University, Novosibirsk 630090, Russia*

Oleg G. Salnikov − *International Tomography Center, SB RAS, Novosibirsk 630090, Russia;* orcid.org/0000-0003-2266-7335

Eduard Y. Chekmenev − *Department of Chemistry, Integrative Biosciences (Ibio), Karmanos Cancer Institute (KCI), Wayne State University, Detroit, Michigan 48202, United States; Russian Academy of Sciences (RAS), Moscow 119991, Russia;* orcid.org/0000-0002-8745-8801

Andrey N. Pravdivtsev − *Department of Radiology and Neuroradiology Section Biomedical Imaging, MOIN CC, Universitätsklinikum Schleswig-Holstein, Kiel 24118, Germany;* orcid.org/0000-0002-8763-617X

Jan-Bernd Hövener − *Department of Radiology and Neuroradiology Section Biomedical Imaging, MOIN CC, Universitätsklinikum Schleswig-Holstein, Kiel 24118, Germany;* orcid.org/0000-0001-7255-7252

Complete contact information is available at: https://pubs.acs.org/10.1021/acs.jpclett.2c02705

Notes

The authors declare the following competing financial interest(s): E.Y.C. declares a stake of ownership in XeUS Technologies, Ltd.

■ ACKNOWLEDGMENTS

A.I.T. and N.V.C. thank the Russian Science Foundation (Grant 21-73-10105) for supporting the SLIC-SABRE experiments and the synthesis of [$^{15}N_1$]fampridine. O.G.S. thanks the Council on Grants of the President of the Russian Federation (Grant MK-2826.2022.1.3) for supporting the optimization of the SABRE conditions. I.V.S., N.V.C., and I.V.K. thank the Russian Science Foundation (Grant 22-43-04426) for supporting SABRE simulations and MRI experiments. The ITC SB RAS team thanks the Russian Ministry of Science and Higher Education for access to NMR/MRI equipment. E.Y.C. is thankful for National Science Foundation Grant CHE-1904780 and National Institutes of Health NIBIB Grant R01EB029829. A.N.P. and J.-B.H. acknowledge funding from the German Federal Ministry of Education and Research (BMBF) within the framework of the e:Med research and funding concept (01ZX1915C), DFG (PR 1868/3-1, HO-4602/2-2, HO-4602/3, GRK2154-2019, EXC2167, FOR5042, and TRR287). MOIN CC was founded by a grant from the European Regional Development Fund (ERDF) and the Zukunftsprogramm Wirtschaft of Schleswig-Holstein (Project 122-09-053).

■ REFERENCES

(1) Heacock, L.; Reig, B.; Lewin, A. A.; Toth, H. K.; Moy, L.; Lee, C. S. Abbreviated Breast MRI: Road to Clinical Implementation. *J. Breast Imaging* **2020**, *2* (3), 201−214.

(2) Ji, S.; Yang, D.; Lee, J.; Choi, S. H.; Kim, H.; Kang, K. M. Synthetic MRI: Technologies and Applications in Neuroradiology. *Magn. Reson. Imaging* **2022**, *55*, 1013−1025.

(3) Voskrebenzev, A.; Vogel-Claussen, J. Proton MRI of the Lung: How to Tame Scarce Protons and Fast Signal Decay. *J. Magn. Reson. Imaging* **2021**, *53* (5), 1344−1357.

(4) Börnert, P.; Norris, D. G. A Half-Century of Innovation in Technology-Preparing MRI for the 21st Century. *Br. J. Radiol.* **2020**, *93*, 20200113.

(5) Zhang, L.; Sun, L.; Lu, Y.; Kuang, Y.; Ling, Z.; Yang, L.; Dong, H.; Yang, S.; Zhao, J.; Song, Y. Molecular Dynamics Simulation and In-Situ MRI Observation of Organic Exclusion during CO_2 Hydrate Growth. *Chem. Phys. Lett.* **2021**, *764*, 138287.

(6) Weiskopf, N.; Edwards, L. J.; Helms, G.; Mohammadi, S.; Kirilina, E. Quantitative Magnetic Resonance Imaging of Brain Anatomy and in Vivo Histology. *Nat. Rev. Phys.* **2021**, *3* (8), 570−588.

(7) Zhao, Z.; Zhen, M.; Zhou, C.; Li, L.; Jia, W.; Liu, S.; Li, X.; Liao, X.; Wang, C. A Gadofullerene Based Liver-Specific MRI Contrast Agent for an Early Diagnosis of Orthotopic Hepatocellular Carcinoma. *J. Mater. Chem. B* **2021**, *9* (28), 5722−5728.

(8) Srivastava, A. K.; Kadayakkara, D. K.; Bar-Shir, A.; Gilad, A. A.; McMahon, M. T.; Bulte, J. W. M. Advances in Using MRI Probes and Sensors for in Vivo Cell Tracking as Applied to Regenerative Medicine. *Dis. Model. Mech.* **2015**, *8* (4), 323−336.

(9) Itatani, K.; Miyazaki, S.; Furusawa, T.; Numata, S.; Yamazaki, S.; Morimoto, K.; Makino, R.; Morichi, H.; Nishino, T.; Yaku, H. New Imaging Tools in Cardiovascular Medicine: Computational Fluid Dynamics and 4D Flow MRI. *Gen. Thorac. Cardiovasc. Surg.* **2017**, *65* (11), 611−621.

(10) Koh, D.-M.; Collins, D. J. Diffusion-Weighted MRI in the Body: Applications and Challenges in Oncology. *Am. J. Roentgenol.* **2007**, *188* (6), 1622−1635.

(11) Padhani, A. R.; Husband, J. E. Dynamic Contrast-Enhanced MRI Studies in Oncology with an Emphasis on Quantification, Validation and Human Studies. *Clin. Radiol.* **2001**, *56* (8), 607−620.

(12) Rosman, K. J. R.; Taylor, P. D. P. Isotopic Compositions of the Elements 1997 (Technical Report). *Pure Appl. Chem.* **1998**, *70* (1), 217−235.

(13) Greenman, R. L.; Smithline, H. A. The Feasibility of Measuring Phosphocreatine Recovery Kinetics in Muscle Using a Single-Shot ^{31}P RARE MRI Sequence. *Acad. Radiol.* **2011**, *18* (7), 917−923.

(14) Menon, R. G.; Xia, D.; Katz, S. D.; Regatte, R. R. Dynamic ^{31}P-MRI and ^{31}P-MRS of Lower Leg Muscles in Heart Failure Patients. *Sci. Rep.* **2021**, *11* (1), 7412.

(15) Semenova, V.; Pavlova, O.; Pirogov, Y. Magnetic Resonance Imaging of Lungs Using Fluorinated Gas. *J. Phys. Conf. Ser.* **2020**, *1439* (1), No. 012043.

(16) Pavlova, O. S.; Anisimov, N. V.; Gervits, L. L.; Gulyaev, M. V.; Semenova, V. N.; Pirogov, Y. A.; Panchenko, V. Y. ^{19}F MRI of Human Lungs at 0.5 T Using Octafluorocyclobutane. *Magn. Reson. Med.* **2020**, *84* (4), 2117−2123.

(17) Couch, M. J.; Ball, I. K.; Li, T.; Fox, M. S.; Biman, B.; Albert, M. S. ^{19}F MRI of the Lungs Using Inert Fluorinated Gases: Challenges and New Developments. *J. Magn. Reson. Imaging* **2019**, *49* (2), 343−354.

(18) Bulte, J. W. M.; Shakeri-Zadeh, A. In Vivo MRI Tracking of Tumor Vaccination and Antigen Presentation by Dendritic Cells. *Mol. Imaging Biol.* **2022**, *24* (2), 198−207.

(19) Witanowski, M. Nitrogen n.m.r. Spectroscopy. *Pure Appl. Chem.* **1974**, *37* (1−2), 225−233.

(20) Webb, A. Increasing the Sensitivity of Magnetic Resonance Spectroscopy and Imaging. *Anal. Chem.* **2012**, *84* (1), 9−16.

(21) Chukanov, N. V.; Shchepin, R. V.; Joshi, S. M.; Kabir, M. S. H.; Salnikov, O. G.; Svyatova, A.; Koptyug, I. V.; Gelovani, J. G.; Chekmenev, E. Y. Synthetic Approaches for ^{15}N-Labeled Hyperpolarized Heterocyclic Molecular Imaging Agents for ^{15}N NMR Signal Amplification by Reversible Exchange in Microtesla Magnetic Fields. *Chem. - Eur. J.* **2021**, *27* (38), 9727−9736.

(22) Shchepin, R. V.; Barskiy, D. A.; Coffey, A. M.; Feldman, M. A.; Kovtunova, L. M.; Bukhtiyarov, V. I.; Kovtunov, K. V.; Goodson, B. M.; Koptyug, I. V.; Chekmenev, E. Y. Robust Imidazole- $^{15}N_2$ Synthesis for High-Resolution Low-Field (0.05 T) ^{15}N Hyperpolarized NMR Spectroscopy. *ChemistrySelect* **2017**, *2* (16), 4478−4483.

(23) Pravdivtsev, A. N.; Yurkovskaya, A. V.; Zimmermann, H.; Vieth, H.-M.; Ivanov, K. L. Enhancing NMR of Insensitive Nuclei by Transfer of SABRE Spin Hyperpolarization. *Chem. Phys. Lett.* **2016**, *661*, 77−82.

(24) Shchepin, R. V.; Barskiy, D. A.; Mikhaylov, D. M.; Chekmenev, E. Y. Efficient Synthesis of Nicotinamide-1−^{15}N for Ultrafast NMR Hyperpolarization Using Parahydrogen. *Bioconjugate Chem.* **2016**, *27* (4), 878−882.

(25) Colell, J. F. P.; Emondts, M.; Logan, A. W. J.; Shen, K.; Bae, J.; Shchepin, R. V.; Ortiz, G. X.; Spannring, P.; Wang, Q.; Malcolmson, S. J.; Chekmenev, E. Y.; Feiters, M. C.; Rutjes, F. P. J. T.; Blümich, B.; Theis, T.; Warren, W. S. Direct Hyperpolarization of Nitrogen-15 in Aqueous Media with Parahydrogen in Reversible Exchange. *J. Am. Chem. Soc.* **2017**, *139* (23), 7761−7767.

(26) Birchall, J. R.; Kabir, M. S. H. H.; Salnikov, O. G.; Chukanov, N. V.; Svyatova, A.; Kovtunov, K. V.; Koptyug, I. V.; Gelovani, J. G.; Goodson, B. M.; Pham, W.; Chekmenev, E. Y. Quantifying the Effects of Quadrupolar Sinks Via 15N Relaxation Dynamics in Metronidazoles Hyperpolarized via SABRE-SHEATH. *Chem. Commun.* **2020**, *56* (64), 9098−9101.

(27) Adams, R. W.; Aguilar, J. A.; Atkinson, K. D.; Cowley, M. J.; Elliott, P. I. P.; Duckett, S. B.; Green, G. G. R.; Khazal, I. G.; Lopez-Serrano, J.; Williamson, D. C. Reversible Interactions with Para-Hydrogen Enhance NMR Sensitivity by Polarization Transfer. *Science* **2009**, *323* (5922), 1708−1711.

(28) Walker, T. G. Fundamentals of Spin-Exchange Optical Pumping. *J. Phys. Conf. Ser.* **2011**, *294* (1), 012001.

https://doi.org/10.1021/acs.jpclett.2c02705
J. Phys. Chem. Lett. 2022, 13, 10253−10260

(29) Schröder, L. Xenon for NMR Biosensing − Inert but Alert. *Phys. Medica* **2013**, *29* (1), 3−16.
(30) Zhang, G.; Hilty, C. Applications of Dissolution Dynamic Nuclear Polarization in Chemistry and Biochemistry. *Magn. Reson. Chem.* **2018**, *56* (7), 566−582.
(31) Ardenkjaer-Larsen, J. H. On the Present and Future of Dissolution-DNP. *J. Magn. Reson.* **2016**, *264*, 3−12.
(32) Fekete, M.; Ahwal, F.; Duckett, S. B. Remarkable Levels of ^{15}N Polarization Delivered through SABRE into Unlabeled Pyridine, Pyrazine, or Metronidazole Enable Single Scan NMR Quantification at the mM Level. *J. Phys. Chem. B* **2020**, *124* (22), 4573−4580.
(33) Robertson, T. B. R.; Clarke, L. J.; Mewis, R. E. Rapid SABRE Catalyst Scavenging Using Functionalized Silicas. *Molecules* **2022**, *27* (2), 332.
(34) Manoharan, A.; Rayner, P. J.; Iali, W.; Burns, M. J.; Perry, V. H.; Duckett, S. B. Achieving Biocompatible SABRE: An in Vitro Cytotoxicity Study. *ChemMedChem.* **2018**, *13* (4), 352−359.
(35) Kidd, B. E.; Gesiorski, J. L.; Gemeinhardt, M. E.; Shchepin, R. V.; Kovtunov, K. V.; Koptyug, I. V.; Chekmenev, E. Y.; Goodson, B. M. Facile Removal of Homogeneous SABRE Catalysts for Purifying Hyperpolarized Metronidazole, a Potential Hypoxia Sensor. *J. Phys. Chem. C* **2018**, *122* (29), 16848−16852.
(36) Barskiy, D. A.; Ke, L. A.; Li, X.; Stevenson, V.; Widarman, N.; Zhang, H.; Truxal, A.; Pines, A. Rapid Catalyst Capture Enables Metal-Free Para-Hydrogen-Based Hyperpolarized Contrast Agents. *J. Phys. Chem. Lett.* **2018**, *9* (11), 2721−2724.
(37) Iali, W.; Olaru, A. M.; Green, G. G. R.; Duckett, S. B. Achieving High Levels of NMR-Hyperpolarization in Aqueous Media With Minimal Catalyst Contamination Using SABRE. *Chem. - A Eur. J.* **2017**, *23* (44), 10491−10495.
(38) Atkinson, K. D.; Cowley, M. J.; Elliott, P. I. P.; Duckett, S. B.; Green, G. G. R.; López-Serrano, J.; Whitwood, A. C. Spontaneous Transfer of Para Hydrogen Derived Spin Order to Pyridine at Low Magnetic Field. *J. Am. Chem. Soc.* **2009**, *131* (37), 13362−13368.
(39) Rayner, P. J.; Burns, M. J.; Olaru, A. M.; Norcott, P.; Fekete, M.; Green, G. G. R.; Highton, L. A. R.; Mewis, R. E.; Duckett, S. B. Delivering Strong ^{1}H Nuclear Hyperpolarization Levels and Long Magnetic Lifetimes through Signal Amplification by Reversible Exchange. *Proc. Natl. Acad. Sci. U. S. A.* **2017**, *114* (16), E3188−E3194.
(40) Pravdivtsev, A. N.; Yurkovskaya, A. V.; Zimmermann, H.; Vieth, H.-M. M.; Ivanov, K. L. Transfer of SABRE-Derived Hyperpolarization to Spin-1/2 Heteronuclei. *RSC Adv.* **2015**, *5* (78), 63615−63623.
(41) Theis, T.; Truong, M.; Coffey, A. M.; Chekmenev, E. Y.; Warren, W. S. LIGHT-SABRE Enables Efficient in-Magnet Catalytic Hyperpolarization. *J. Magn. Reson.* **2014**, *248*, 23−26.
(42) Barskiy, D. A.; Shchepin, R. V.; Coffey, A. M.; Theis, T.; Warren, W. S.; Goodson, B. M.; Chekmenev, E. Y. Over 20% ^{15}N Hyperpolarization in Under One Minute for Metronidazole, an Antibiotic and Hypoxia Probe. *J. Am. Chem. Soc.* **2016**, *138* (26), 8080−8083.
(43) Salnikov, O. G.; Chukanov, N. V.; Svyatova, A.; Trofimov, I. A.; Kabir, M. S. H.; Gelovani, J. G.; Kovtunov, K. V.; Koptyug, I. V.; Chekmenev, E. Y. ^{15}N NMR Hyperpolarization of Radiosensitizing Antibiotic Nimorazole via Reversible Parahydrogen Exchange in Microtesla Magnetic Fields. *Angew. Chemie Int. Ed.* **2021**, *60* (5), 2406−2413.
(44) Shchepin, R. V.; Truong, M. L.; Theis, T.; Coffey, A. M.; Shi, F.; Waddell, K. W.; Warren, W. S.; Goodson, B. M.; Chekmenev, E. Y. Hyperpolarization of "Neat" Liquids by NMR Signal Amplification by Reversible Exchange. *J. Phys. Chem. Lett.* **2015**, *6* (10), 1961−1967.
(45) Theis, T.; Truong, M. L.; Coffey, A. M.; Shchepin, R. V.; Waddell, K. W.; Shi, F.; Goodson, B. M.; Warren, W. S.; Chekmenev, E. Y. Microtesla SABRE Enables 10% Nitrogen-15 Nuclear Spin Polarization. *J. Am. Chem. Soc.* **2015**, *137* (4), 1404−1407.
(46) Pravdivtsev, A. N.; Kempf, N.; Plaumann, M.; Bernarding, J.; Scheffler, K.; Hövener, J.; Buckenmaier, K. Coherent Evolution of Signal Amplification by Reversible Exchange in Two Alternating Fields (Alt-SABRE). *ChemPhysChem* **2021**, *22* (23), 2381−2386.
(47) Ariyasingha, N. M.; Lindale, J. R.; Eriksson, S. L.; Clark, G. P.; Theis, T.; Shchepin, R. V.; Chukanov, N. V.; Kovtunov, K. V.; Koptyug, I. V.; Warren, W. S.; Chekmenev, E. Y. Quasi-Resonance Fluorine-19 Signal Amplification by Reversible Exchange. *J. Phys. Chem. Lett.* **2019**, *10* (15), 4229−4236.
(48) Theis, T.; Ariyasingha, N. M.; Shchepin, R. V.; Lindale, J. R.; Warren, W. S.; Chekmenev, E. Y. Quasi-Resonance Signal Amplification by Reversible Exchange. *J. Phys. Chem. Lett.* **2018**, *9* (20), 6136−6142.
(49) Pravdivtsev, A. N.; Skovpin, I. V.; Svyatova, A. I.; Chukanov, N. V.; Kovtunova, L. M.; Bukhtiyarov, V. I.; Chekmenev, E. Y.; Kovtunov, K. V.; Koptyug, I. V.; Hövener, J.-B. Chemical Exchange Reaction Effect on Polarization Transfer Efficiency in SLIC-SABRE. *J. Phys. Chem. A* **2018**, *122* (46), 9107−9114.
(50) Knecht, S.; Kiryutin, A. S.; Yurkovskaya, A. V.; Ivanov, K. L. Efficient Conversion of Anti-Phase Spin Order of Protons into ^{15}N Magnetisation Using SLIC-SABRE. *Mol. Phys.* **2019**, *117*, 2762−2771.
(51) Chukanov, N. V.; Salnikov, O. G.; Trofimov, I. A.; Kabir, M. S. H.; Kovtunov, K. V.; Koptyug, I. V.; Chekmenev, E. Y. Synthesis and ^{15}N NMR Signal Amplification by Reversible Exchange of [^{15}N]-Dalfampridine at Microtesla Magnetic Fields. *ChemPhysChem* **2021**, *22* (10), 960−967.
(52) Hayes, K. C. The Use of 4-Aminopyridine (Fampridine) in Demyelinating Disorders. *CNS Drug Rev.* **2004**, *10* (4), 295−316.
(53) Broicher, S. D.; Filli, L.; Geisseler, O.; Germann, N.; Zörner, B.; Brugger, P.; Linnebank, M. Positive Effects of Fampridine on Cognition, Fatigue and Depression in Patients with Multiple Sclerosis over 2 Years. *J. Neurol.* **2018**, *265* (5), 1016−1025.
(54) Skovpin, I. V.; Svyatova, A.; Chukanov, N.; Chekmenev, E. Y.; Kovtunov, K. V.; Koptyug, I. V. ^{15}N Hyperpolarization of Dalfampridine at Natural Abundance for Magnetic Resonance Imaging. *Chem. - Eur. J.* **2019**, *25* (55), 12694−12697.
(55) DeVience, S. J.; Walsworth, R. L.; Rosen, M. S. Preparation of Nuclear Spin Singlet States Using Spin-Lock Induced Crossing. *Phys. Rev. Lett.* **2013**, *111* (17), 173002.
(56) Cowley, M. J.; Adams, R. W.; Atkinson, K. D.; Cockett, M. C. R.; Duckett, S. B.; Green, G. G. R.; Lohman, J. A. B.; Kerssebaum, R.; Kilgour, D.; Mewis, R. E. Iridium N-Heterocyclic Carbene Complexes as Efficient Catalysts for Magnetization Transfer from Para-Hydrogen. *J. Am. Chem. Soc.* **2011**, *133* (16), 6134−6137.
(57) Knecht, S.; Pravdivtsev, A. N.; Hövener, J.-B.; Yurkovskaya, A. V.; Ivanov, K. L. Quantitative Description of the SABRE Process: Rigorous Consideration of Spin Dynamics and Chemical Exchange. *RSC Adv.* **2016**, *6* (29), 24470−24477.
(58) Svyatova, A.; Skovpin, I. V.; Chukanov, N. V.; Kovtunov, K. V.; Chekmenev, E. Y.; Pravdivtsev, A. N.; Hövener, J.; Koptyug, I. V. ^{15}N MRI of SLIC-SABRE Hyperpolarized ^{15}N-Labelled Pyridine and Nicotinamide. *Chem. - Eur. J.* **2019**, *25* (36), 8465−8470.
(59) Pravdivtsev, A. N.; Hövener, J. B. Simulating Non-Linear Chemical and Physical (CAP) Dynamics of Signal Amplification By Reversible Exchange (SABRE). *Chem. - Eur. J.* **2019**, *25*, 7659−7668.
(60) Pravdivtsev, A. N.; Brahms, A.; Ellermann, F.; Stamp, T.; Herges, R.; Hövener, J. Parahydrogen-Induced Polarization and Spin Order Transfer in Ethyl Pyruvate at High Magnetic Fields. *Sci. Rep.* **2022**, DOI: 10.1038/s41598-022-22347-1.
(61) Khan, A. S.; Harvey, R. L.; Birchall, J. R.; Irwin, R. K.; Nikolaou, P.; Schrank, G.; Emami, K.; Dummer, A.; Barlow, M. J.; Goodson, B. M.; Chekmenev, E. Y. Enabling Clinical Technologies for Hyperpolarized ^{129}Xenon Magnetic Resonance Imaging and Spectroscopy. *Angew. Chemie - Int. Ed.* **2021**, *60* (41), 22126−22147.
(62) Shepelytskyi, Y.; Hane, F. T.; Grynko, V.; Li, T.; Hassan, A.; Albert, M. S. Hyperpolarized ^{129}Xe Time-of-Flight MR Imaging of Perfusion and Brain Function. *Diagnostics* **2020**, *10* (9), 630.
(63) Cunningham, C. H.; Lau, J. Y. C.; Chen, A. P.; Geraghty, B. J.; Perks, W. J.; Roifman, I.; Wright, G. A.; Connelly, K. A.

Hyperpolarized ^{13}C Metabolic MRI of the Human Heart. *Circ. Res.* **2016**, *119* (11), 1177−1182.

(64) Nelson, S. J.; Kurhanewicz, J.; Vigneron, D. B.; Larson, P. E. Z.; Harzstark, A. L.; Ferrone, M.; van Criekinge, M.; Chang, J. W.; Bok, R.; Park, I.; Reed, G.; Carvajal, L.; Small, E. J.; Munster, P.; Weinberg, V. K.; Ardenkjaer-Larsen, J. H.; Chen, A. P.; Hurd, R. E.; Odegardstuen, L.-I.; Robb, F. J.; Tropp, J.; Murray, J. A. Metabolic Imaging of Patients with Prostate Cancer Using Hyperpolarized [1−^{13}C]Pyruvate. *Sci. Transl. Med.* **2013**, *5* (198), 198ra108−198ra108.

https://doi.org/10.1021/acs.jpclett.2c02705
J. Phys. Chem. Lett. 2022, 13, 10253−10260